ADVANCED NANOMECHANICAL TESTING

Controlling the high temperature deformation behavior and thermal stability of ultra-fine-grained W by re alloying

Johann Kappacher[1,a], Oliver Renk[2], Daniel Kiener[1], Helmut Clemens[1], Verena Maier-Kiener[1]

[1] *Department of Materials Science, Montanuniversität Leoben, Leoben, Austria*
[2] *Erich Schmid Insitute of Materials Science, Austrian Academy of Sciences, Leoben, Austria*
[a] Address all correspondence to this author. e-mail: johann.kappacher@unileoben.ac.at

Verena Maier-Kiener was an editor of this journal during the review and decision stage. For the JMR policy on review and publication of manuscripts authored by editors, please refer to http://www.mrs.org/editor-manuscripts/.

Due to their outstanding properties, ultra-fine-grained tungsten and its alloys are promising candidates to be used in harsh environments, hence it is crucial to understand their high temperature behavior and underlying deformation mechanisms. Therefore, advanced nanoindentation techniques were applied to ultra-fine-grained tungsten–rhenium alloys up to 1073 K. A continuous hardness decrease up to 0.2 T_m is rationalized by a still dominating effect of the Peierls stress. However, the absence of well-established effects of Rhenium alloying, resulting in a reduced temperature dependence of strength for coarse-grained microstructures, was interpreted as an indication for a diminishing role of kink-pair formation in ultra-fine-grained metals with sufficiently fine grain size. Despite slight grain growth in W, dislocation–grain boundary interaction was identified as the dominating deformation mechanism above 0.2 T_m. Interaction and accommodation of lattice dislocations with grain boundaries was affected by a reduced boundary diffusivity through alloying with Re.

Introduction

Driven by increased requirements for high-performance applications, material developments tend towards the use of refined microstructures, as according to Hall and Petch [1, 2] the strength of a material can be increased that way. Severe plastic deformation techniques [3–6] enable synthesis of ultra-fine-grained (ufg) and nanocrystalline (nc) materials on a bulk scale, hence the properties of such materials were studied with growing interest [7–10].

For the development of plasma-facing components in nuclear fusion reactors, body-centered cubic (bcc) tungsten is a promising candidate due to its exceptional physical properties [11, 12]. With a high melting point, T_m, of 3695 K, good resistance for void swelling or sputtering as well as good thermal conductivity, which remains stable under irradiation, it is ideal for applications in such harsh environments [13, 14]. Decreasing the grain size to the ufg or nc regime even improves the radiation tolerance, as grain boundaries act as sinks for defects [15,

16]. The effect of the alloying element Rhenium is of particular interest, as due to a change of the core structure of the screw dislocations, ductility at ambient temperature can be improved [17, 18]. On the other hand, when W faces such nuclear environments it will be transmuted, resulting in an increase in Re content [19]. Re strongly influences the deformation behavior of coarse-grained (cg) W at low temperatures [17, 18]. It induces a transition from a symmetric to an asymmetric core of the $1/2\langle 111 \rangle$ screw dislocation and leads to a reduction of the Peierls barrier [20]. For cg W alloying with Re results in a reduced temperature and strain rate sensitivity of the hardness and an increased activation volume below 0.2 T_m [21]. To fully utilize the considerable strengthening effect of ufg materials, it is therefore necessary to understand the combined influence of grain boundaries and Re content on the mechanical properties and the underlying deformation behavior, especially at high temperatures. To identify the rate controlling mechanisms of plastic deformation, important parameters such as the strain

rate sensitivity, *m*, and the corresponding (apparent) activation volume, V^*, can be determined [22]. The latter is commonly normalized to the cubed Burgers vector b^3 in order to facilitate comparison between different materials.

In conventional cg face-centered cubic (fcc) metals, a rather low *m* of around 10^{-3} and V^*-values of a few $100b^3$ are observed [23–25]. This indicates that dislocation–dislocation interactions such as cutting of forest dislocations are the rate controlling deformation mechanism [26]. With a decrease of the grain size to submicron or nanoscaled dimensions, intragranular dislocation interactions vanish. Here, emission or absorption processes of dislocations at grain boundaries become important. Accordingly, the resulting strain rate sensitivity increases by about an order of magnitude [23, 24], while V^* decreases to a few $10b^3$ [27, 28]. This is indicative of a change of the deformation mode from dislocation–dislocation to dislocation–grain boundary interactions [26]. The observed strain rate sensitivity is rather temperature independent up to 0.2 to 0.3 T_m [29–32], but increases as temperature rises. The cause of this behavior is thermally activated accommodation of lattice dislocations within the grain boundaries [33, 34] with increasing temperatures.

For bcc metals the flow stress below 0.2 T_m is composed of a thermal as well as an athermal part [22, 35]. The thermal contribution originates from the non-planar core structure of the $1/2\langle 111 \rangle$ screw dislocations, resulting in a limited mobility compared to edge dislocations. Hence, the movement of screw dislocations via the kink-pair mechanism is the rate limiting step for deformation [36]. The resulting pronounced strain rate sensitivity for cg or single-crystalline (sx) bcc metals was intensively investigated for Cr (*m* = 0.02–0.07) [37–39], but also for other bcc elements such as Fe (*m* = 0.05) [28], Ta (*m* = 0.06) [28], V (*m* = 0.045) [28, 40], and W (*m* = 0.02–0.03) [21, 41].

Different to fcc metals, a decrease in grain size reduces the strain rate sensitivity of bcc metals [28, 38–40, 42, 43]. This is generally attributed to a major strengthening contribution from grain refinement, providing rather athermal, long-range obstacles for dislocations, while the local Peierls barrier provides only limited contribution to the overall strength [37, 43, 44]. The corresponding activation volumes are reported to be below $10b^3$. Commonly this is associated with the kink-pair mechanism being still active, independent of the grain size during plastic deformation at low temperatures [28, 39, 41].

Overcoming 0.2 T_m, the kink pairs are fully thermally activated, screw and edge dislocations exhibit the same mobility and only athermal barriers contribute to the materials strength [35]. For cg materials, this implies a reduced strain rate sensitivity at the order of 10^{-3} and activation volumes above $100b^3$ depending on the dislocation density, suggesting dislocation–dislocation interactions to remain the rate controlling process [21, 36]. Contrary, ufg bcc materials show an increased rate sensitivity and activation volumes of a few $10b^3$ above this critical temperature.

This indicates a behavior similar to ufg fcc metals, where dislocation–grain boundary interactions dominate plastic deformation [37, 39, 41].

To expand the current understanding regarding microstructural stability as well as the influence of alloying on the thermally activated deformation mechanisms in ufg bcc metals, this work aims to investigate the deformation behavior of ufg W and W–Re alloys. Therefore, high temperature (HT) nanoindentation experiments are utilized to access dominating deformation mechanisms of these materials up to 1073 K, while high-resolution electron microscopy and static annealing treatments were conducted to analyze the microstructural stability in dependence of the Re content.

Results

Figure 1 represents back-scattered electron (BSE) images as well as colored inverse pole figure (IPF) maps obtained from electron back-scatter diffraction (EBSD) of the investigated high-pressure torsion (HPT)-deformed materials before HT nanoindentation. The equivalent plastic strains are indicated in the respective image. A cumulative distribution plot of the grain size indicates very comparable characteristics with average grain sizes of around 250, 250, and 280 nm for W, W5Re, and W10Re (composition in wt%), respectively. As typical for HPT-deformed samples [45], the majority of the grain boundaries (> 86%) have a high-angle character, i.e., misorientation angles > 15°.

In Fig. 2, EBSD and BSE micrographs of the as-deformed and heat treated samples are presented. Additionally, cumulative distribution plots of the grain size evolution with annealing temperature are shown. Due to the slightly different plastic strains achieved during the HPT deformation process, the samples intended for the annealing experiments exhibit marginally different grain sizes (see section 5: Methodology). W has a grain size of around 290 nm in the as-HPT deformed state and shows slight grain growth to 320 nm already after annealing at 1073 K for 120 min. The selected annealing time corresponds to the holding time used for thermal stabilization during the HT nanoindentation experiments. W5Re, which has been subjected to the same equivalent strain in the HPT process, has a smaller grain size of around 230 nm, but grain growth to 270 nm starts only at 1273 K when annealed for 120 min. Due to the reduced strain that could be applied in case of W10Re, the grain size variation between the different samples is larger, but around 230 nm in the as-deformed state. Similar to the W5Re samples, significant grain growth was detected only at 1273 K, causing an increase to 280 nm after a holding time of 120 min.
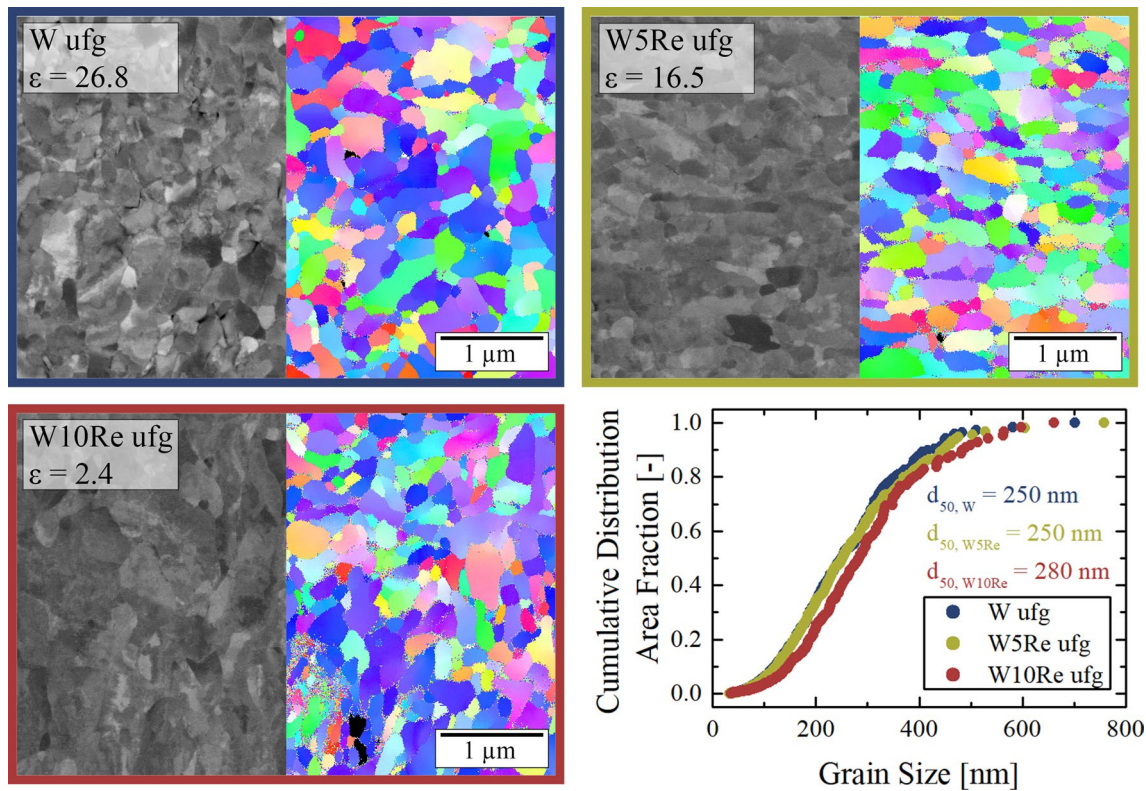
Figure 1: Microstructures (axial direction) of the investigated ufg W–Re alloys. The left side of the micrographs represents SEM images taken in BSE contrast, while the right sides are EBSD grain orientation maps. The mean grain sizes are indicated in the cumulative distribution plots. The shear direction of the HPT process is horizontal in all images.

RT hardness of the heat-treated samples measured by nanoindentation as a function of annealing temperature is illustrated in Fig. 3. In the as-HPT condition, hardness values of 11.10 ± 0.17 GPa, 12.09 ± 0.15 GPa , and 10.59 ± 0.28 GPa for W, W5Re, and W10Re, respectively, were measured. Annealing the W samples at 723 K and 773 K does not result in any notable changes in hardness, while at 873 K a slight decrease of 4 % followed by a significant drop of 15 % at 1073 K was observed. For the alloyed variants, no significant hardness reduction was detected up to 1173 K. Annealing at 1273 K, however, results in a decrease of 6 % and 11 % for W5Re and W10Re, respectively, in line with the grain size measurements.

In Fig. 4, representative indentation data are shown for ufg W at RT, 673 K and 1073 K. From the load displacement curves in Fig. 4a, a distinct thermal dependence of hardness can be already noticed. The continuously recorded Young's moduli, E, show rather constant values over indentation depth and are in line with bulk data from Lowrie et al. [46], Fig. 4b. Figure 4c shows representative hardness versus displacement curves for both, constant strain rate as well as strain rate jump tests. A clear reduction in hardness with temperature is seen, while no influence of the testing protocol is evident.

The evolution of hardness, H, over homologous temperature based on the constant indentation strain rate experiments are displayed in Fig. 5a. The melting temperatures are 3695 K, 3493 K, and 3418 K for W, W5Re, and W10Re, respectively [47]. For comparison, the temperature-dependent hardness of the cg counterparts is presented in Fig. 5b [21]. Starting from very similar values at RT (11.64 ± 0.21 GPa, 11.51 ± 0.09 GPa , and 11.19 ± 0.21 GPa for W, W5Re, and W10Re, respectively) a strong decrease in hardness with testing temperature can be observed for all three materials. While for ufg W a steady decrease occurs over the whole testing temperature range, the hardness for W5Re and W10Re reaches a rather constant level for temperatures above 673 K.

The results of the strain rate jump tests and the derived activation parameters are shown in Fig. 6. The strain rate sensitivity, m (Fig. 6a) exhibits two apparent regimes. At low temperatures, a constant strain rate sensitivity, independent of temperature and alloying elements, around 0.01 is observed. At higher temperatures, however, a pronounced increase of strain rate sensitivity with temperature can be detected. The temperature between these two regimes is shifted towards higher values with increasing Re content. With a linear fit the transition temperatures were estimated to be 600, 810, and 900 K for W, W5Re,
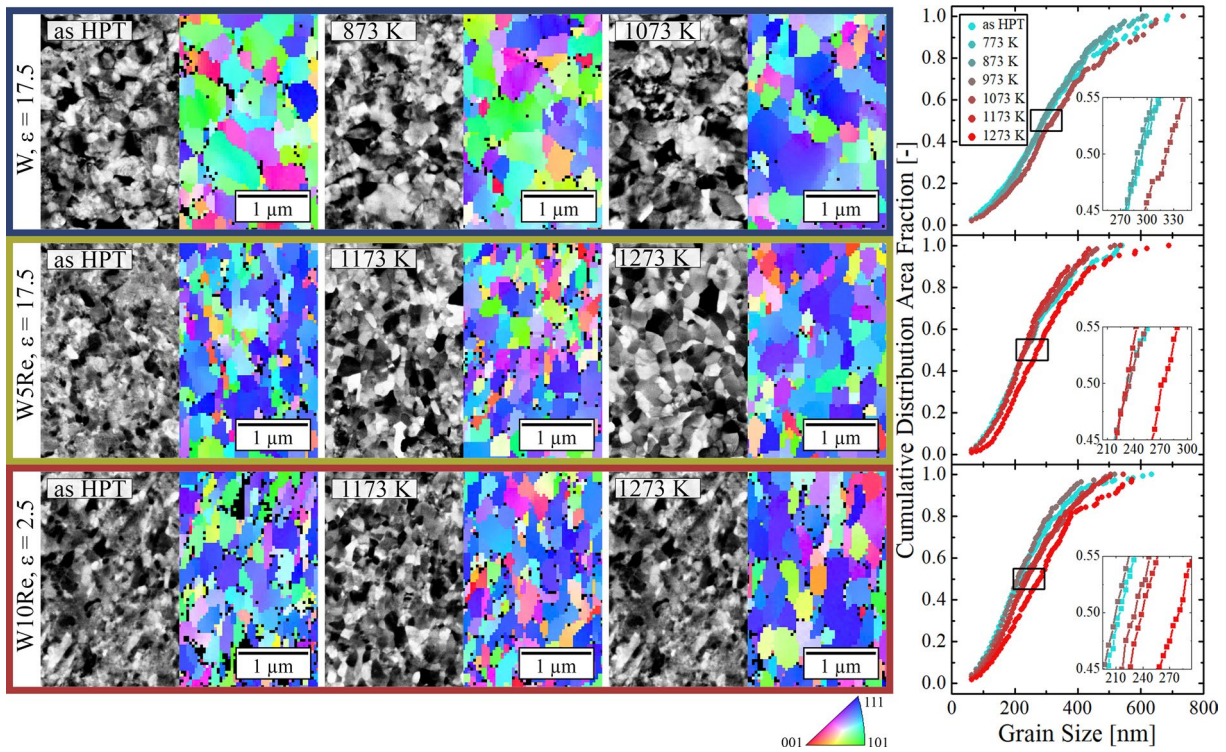
Figure 2: Microstructural evolution of W, W5Re, and W10Re after annealing represented with SEM/BSE and EBSD micrographs. While W exhibits significant grain growth at 1073 K, W5Re and W10Re are thermally stable up to 1173 K. The duration of the heat treatment was 120 min for each indicated annealing temperature.
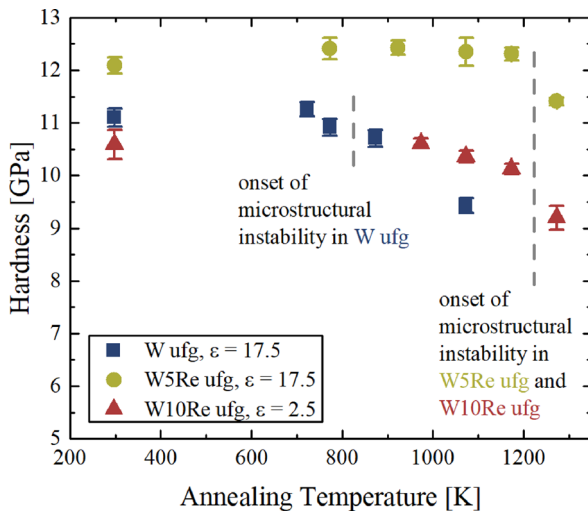

Figure 3: Evolution of RT hardness of the investigated materials as a function of annealing temperature. The duration of the heat treatments was fixed to 120 min, which corresponds to the average settle time to lower thermal drift during the HT nanoindentation experiments. While ufg W exhibits a significant decrease in hardness starting from 873 K, W5Re and W10Re are thermally stable up to 1173 K.

and W10Re, respectively. The calculated activation volumes, V^*, in Fig. 6b are slightly below $10b^3$ at RT. With increasing

temperature the activation volume rises independent of the Re content. For comparison, the activation volumes of the same material but in its cg condition are plotted in the same diagram [21]. While for the cg state V^* continuously increases, for the ufg states above 0.2 T_m the activation volume remains constant or even slightly decreases. In the high temperature regime, W shows a lower activation volume of $19 \pm 6b^3$, when compared to W5Re ($30 \pm 11b^3$) and W10Re ($37 \pm 15b^3$). The third activation parameter that can be extracted from nanoindentation experiments to identify the rate controlling mechanism is the activation energy for plastic flow, Q.

$$Q \approx \Delta\mathscr{H} = \frac{H \cdot V^*}{\sqrt{3} \cdot C^* \cdot T} \cdot \frac{\partial(\ln H)}{\partial(1/T)}. \tag{1}$$

It was approximated by the apparent activation enthalpy, $\Delta\mathscr{H}$, according to Eq. 1, introduced by Lee et al. [48], where C^* is a constraint factor of 2.8. The results are plotted as a function of temperature in Fig. 6c. Below 0.2 T_m values of 1.0 ± 0.5, 1.6 ± 0.7, and 1.0 ± 0.3 eV for W, W5Re, and W10Re were calculated, respectively. Above this critical temperature the two alloys exhibit low values of 0.2 ± 0.1 eV (W5Re) and 0.3 ± 0.1 eV (W10Re), while in ufg W an increased activation energy of 2.6 ± 0.9 eV can be observed.
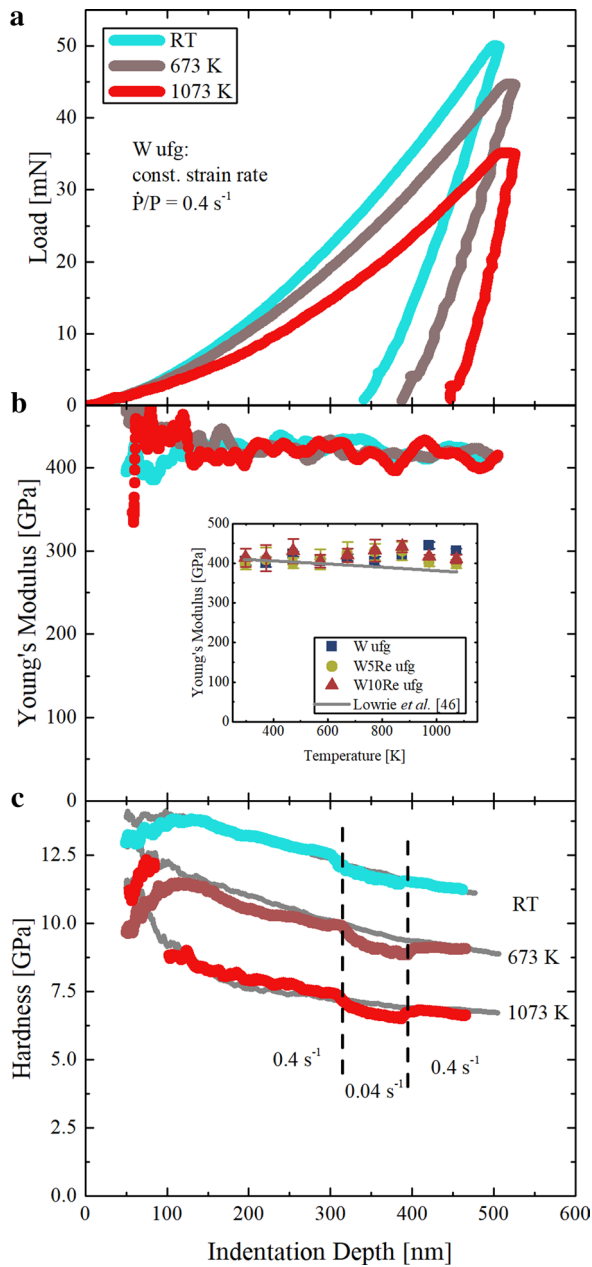
Figure 4: Representative indentation data for ufg W at RT, 673 K and 1073 K: (a) load displacement curves, (b) Young's modulus, and (c) hardness plotted over indentation depth for indents performed with constant indentation strain rate. The inset in (b) shows the evolution of the Young's modulus with temperature and additional literature data for pure W [46]. In (c) selected curves from the strain rate jump tests are presented in addition.

Discussion

Regarding the microstructure of the HPT-deformed materials, Fig. 1 reveals that in all cases the grain shape is globular or slightly elongated along the shear direction (horizontally) and the misorientation angle of the majority of boundaries is larger than 15°, i.e., they are high-angle grain boundaries [45].
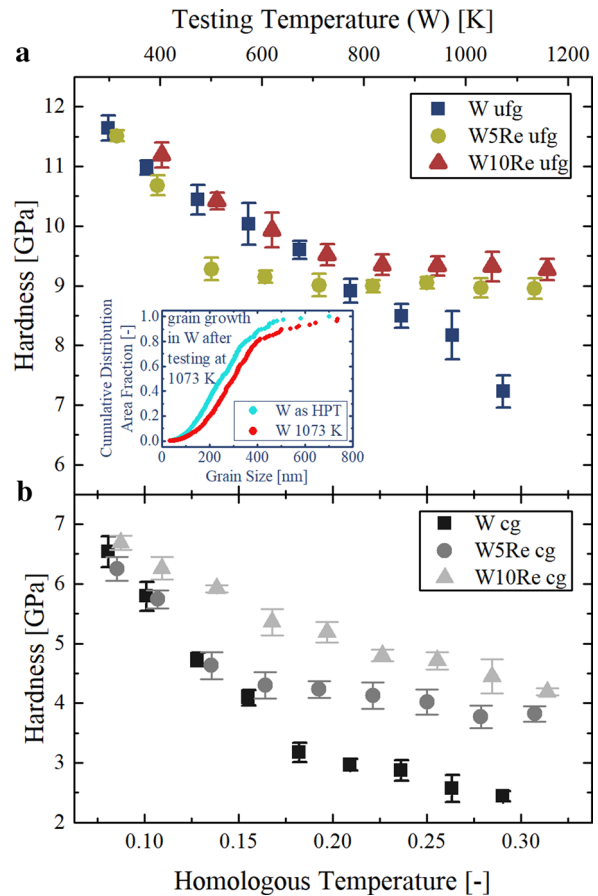

Figure 5: (a) Evolution of hardness over testing temperature for the three investigated materials at constant indentation strain rates. W5Re and W10Re show a pronounced athermal deformation regime, while for W a gradual decrease of hardness over temperature can be observed. In (b) previously reported data for the same materials in cg condition [21] are presented for comparison.

Although different strains were applied to the three material variants, their grain sizes are almost identical. Also, the misorientation distribution for the different materials (not shown here) are qualitatively the same. Therefore, the grain boundary characters can be regarded as similar, allowing to assess the influence of Re alloying on the underlying deformation processes and the microstructural stability.

Static heat treatments regarding the microstructural evolution and RT hardness presented in Figs. 2 and 3 show that concerning the grain size of the ufg W samples a saturation of microstructural refinement is almost reached for strains of $\varepsilon = 17.5$, as higher strains do not cause significant further refinement—290 nm versus 250 nm after $\varepsilon = 26.8$. The hardness of ufg W decreases slightly starting already at annealing temperatures of 873 K. In contrast to the hardness measurements, the grain size derived from EBSD measurements revealed significant grain growth starting at 1073 K after annealing for 120 min. A possible explanation could be that
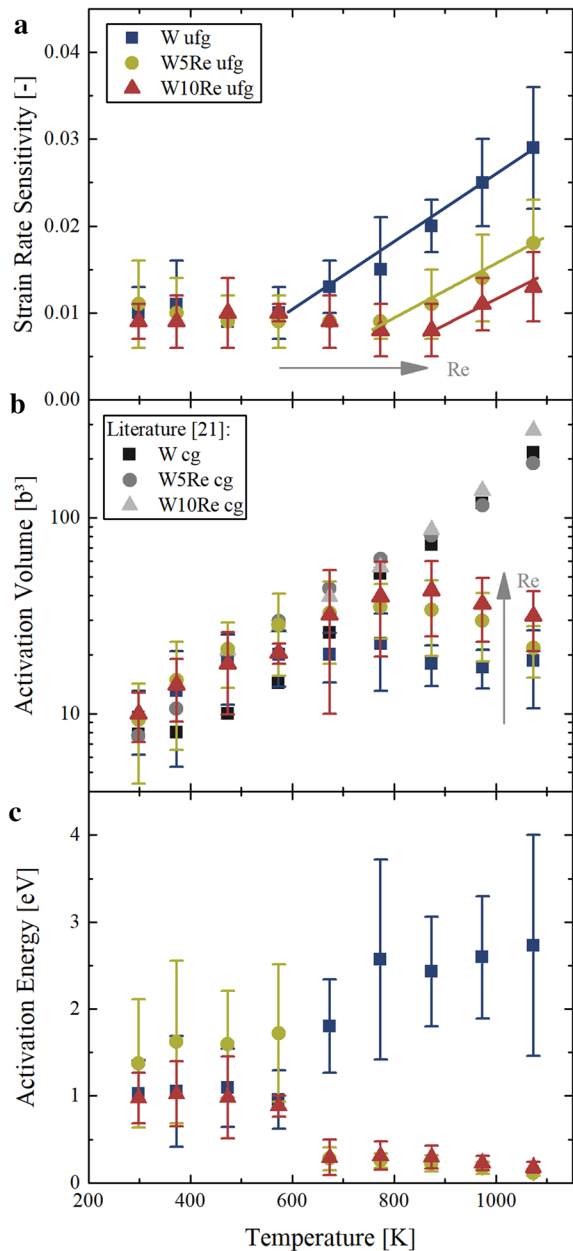
Figure 6: (a) Strain rate sensitivity, (b) activation volume, and (c) activation energy as a function of testing temperature. At temperatures below 673 K all three material parameters are unaffected by the alloying content. Re shifts the temperature, upon which *m* increases to higher values, while V^* is affected by the Re content at elevated testing temperatures. The activation volume for the three materials in cg condition is added for comparison [21]. At high temperatures the two alloys show a reduced, while ufg W exhibits an increased activation energy when compared to the values obtained below 0.2 T_m.

the step size for EBSD measurements of 40 nm impedes detection of slight grain growth events. This means that hardness measurements are more sensitive to slight microstructural changes that are not easily accessible by EBSD. Compared to pure W, the alloyed sample W5Re was found to be thermally

stable up to 1173 K. Here, grain growth accompanied by a hardness decrease starts at 1273 K. For W10Re, however, a stronger scatter for both, hardness and grain size, can be noticed. Probing different W10Re samples at the same strain before annealing revealed slightly different hardness values, reflected in a more prominent error bar. This can be attributed to the reduced equivalent strains that could be realized during HPT in the case of W10Re, being far from saturation (at least $\varepsilon > 17$ required), resulting in a less homogeneous microstructure. Similarly, the slight decrease of hardness for W10Re at annealing temperatures up to 1173 K (Fig. 3) as well as the scatter in grain size (Fig. 2) can be attributed to the prevailing inhomogeneous microstructure. Nevertheless, the thermal stability is similar to W5Re, with significant grain growth starting only at about 1273 K. The increase in thermal stability for W5Re and W10Re can be associated with the influence of solute atoms on the grain boundary mobility. An atmosphere of solute atoms is associated with the grain boundary and its velocity is then controlled by the diffusion rate of the solute atoms in the bulk material, rather than by grain boundary diffusion in pure metals [49].

The constant Young's modulus over indentation depth (Fig. 4) and its excellent agreement with literature data is a strong quantitative validation of our HT nanoindentation data. Notably, at 1073 K the measured Young's modulus is about 15% higher compared to Ref. [46], which could arise from an increased pile-up behavior of the ufg materials at higher testing temperature [50]. Alloying with Re has no measurable effect on the Young's modulus, as supported by the results of Ayres et al. [51], who demonstrated that addition of 10 % Re has a negligible effect on the Young's modulus (i.e., 1.5 % at RT), which is below the standard deviations in our measurements. Hence, it is reasonable that the temperature dependence of the Young's modulus in W–Re alloys is similar to pure W as seen in the present HT nanoindentation results.

Although the RT hardness values of the HT nanoindentation samples (Fig. 5a) are at a similar level, pure W and W5Re are slightly harder than W10Re. This can again be attributed to the slightly larger grain size of the W10Re sample and hence a reduced Hall–Petch hardening [1, 2]. Comparing the hardness values of W and the two Re-alloyed variants over temperature, a very different behavior is observed. Commonly, cg metals with a bcc crystal structure show a drastically decreasing flow stress or hardness as temperature approaches ∼ 0.2 T_m, where a rather constant plateau value is reached [22, 35] (compare Fig. 5b, data taken from Ref. [21]). In contrast, the ufg W sample shows a steady decrease of hardness over temperature without the occurrence of a pronounced athermal hardness plateau. Similar results were reported by Bonk et al. [52], who investigated cold-rolled W with a grain size of 240 nm using high temperature tensile tests. Inspecting the microstructure after testing at

1073 K, grain growth from 250 to 300 nm could be noticed, as indicated in the inset in Fig. 5a. This thermally induced grain growth matches with the results of the static heat treatments (Fig. 3) and explains the absence of an athermal plateau and the observed continuous hardness decrease with increasing testing temperatures, respectively. A different behavior can be observed for the alloyed materials, where the Re atoms stabilize the ufg microstructure and suppress thermally induced grain growth up to the maximum testing temperature and an athermal plateau is evident. Although the grain size of W10Re is larger (280 nm compared to 250 nm) the athermal hardness level with 9.3 GPa is slightly higher compared to 9.0 GPa for W5Re. This increase can be associated with a solution hardening effect of Re, as observed for the cg counterparts at high temperatures [21]. However, comparing the athermal hardness plateau with cg W, W5Re, and W10Re in Fig. 5b, a clearly different behavior can be observed. For testing temperatures exceeding $\sim 0.2\,T_m$, the ufg alloys reveal a truly athermal hardness plateau, where hardness becomes temperature invariant. In case of cg materials, however, hardness decreases further by about 20 % at these temperatures. Above $0.2\,T_m$ dislocation motion and hence plastic deformation should be temperature independent, except for the contribution of the shear modulus, which only reduces marginally by 4 % within the temperature interval discussed. However, when using a Berkovich indenter, equivalent strains of 7.16 % are realized [53]. Hence, a sufficient number of dislocations and so work hardening is involved at low T_m, which becomes subdued at elevated temperatures due to dynamic recovery processes, reflected in decreasing hardness values. This is in line with work from Nemat-Nasser et al. [54, 55] showing that for cg Mo and Nb the work-hardening rate in a temperature range of 0.2 to 0.3 T_m decreases, i.e., dynamic recovery increases with temperature. As pronounced dislocation interactions are widely absent in the ufg W5Re and W10Re microstructures, a truly athermal behavior without any hardness reduction can be observed.

The rather similar transition temperatures just below 0.2 T_m in Fig. 5 for both the cg and ufg materials point towards the same mechanism responsible for the strong temperature dependence at low homologous temperatures. The activation volume, an indicator for the rate controlling process, is also very similar for both material states below 0.2 T_m (Fig. 6b). The respective average activation energies for plastic deformation are well within the range for kink-pair formation, where values between 1.10 and 1.75 eV are reported [56–59]. Taken together, these results point towards kink-pair formation as the rate controlling deformation mechanism below 0.2 T_m.

However, despite that, a main fingerprint of Re alloying is absent for the ufg condition. Due to its reduction of the Peierls potential [20] for cg W–Re alloys, the temperature dependence of hardness as well as strain rate sensitivity and activation energy for plasticity are reduced below 0.2 T_m [60]. While these trends

are well reproduced for the cg W–Re alloys [21], using the same experimental setup, it is not captured for the ufg conditions. This could be an indication that for bcc metals with a sufficiently fine grain size, the high shear stresses necessary for plastic deformation enhance screw dislocation mobility and the role of kink-pair formation as the rate controlling step for plasticity diminishes [61]. In fact, the stresses necessary to deform the ufg W and W–Re samples are almost twice as high compared to those required to deform the cg states (i.e., to form kink pairs). These high stresses could facilitate mechanically driven kink-pair formation even at low temperatures.

The strain rate sensitivity tends to increase noticeably above a certain temperature, Fig. 6a. For such fine-grained metals, the rate controlling processes above a critical temperature seem to be related to the interaction of dislocations with grain boundaries, either during propagation or the subsequent accommodation process [34]. The latter one, also referred to as intergranular stress relaxation, can be thermally facilitated above some temperature, explaining the increasing rate dependence of mechanical properties. Different accommodation processes are proposed in literature, for instance dissociation, core delocalization, or incorporation. A delocalization of the dislocation core also leads to a thermal activation factor below 0.2 T_m although in this case the process would be mechanically driven. However, in any case the relaxation time scales inversely to the grain boundary diffusion coefficient [62]. This is consistent with our data, as the temperature where m rises is shifted towards higher values with increasing Re content, due to the reduction of grain boundary diffusivity. Hence, higher temperatures are required for these diffusion-controlled processes which increase the strain rate sensitivity. In line, also a comparison of the activation volumes between cg and ufg samples suggests a difference in the rate controlling mechanism for the ufg variants above the transition temperature as temperatures exceed 0.2 T_m. In fact, V^* remains rather constant or to some extent even decreases slightly. A value of a few ten b^3 as well as an increased strain rate sensitivity points towards dislocation–grain boundary interaction as the dominant deformation mechanism [39]. Even though the grain size of W at 1073 K eventually becomes larger than W10Re, the activation volume is not significantly affected, as the grain size is still too small for extended dislocation storage and interaction. While according to Eq. 4 a higher hardness would lead to a lower activation volume in case of ufg W10Re, the addition of Re retards the thermal activation of dislocation–grain boundary interactions represented by a lower strain rate sensitivity. This contribution is stronger in the present case, thus leading to a higher activation volume for the alloyed material variants. We therefore conclude that alloying with Re intrinsically shifts the activation volume in ufg W to higher values at elevated temperatures. A possible explanation would be the effect of Re alloying on the core of screw dislocations [20]. Screw and edge

dislocations have similar velocities through thermal activation above 0.2 T_m. However, a contracted core of screw dislocations in case of the alloyed materials would give them a higher mobility, which eventually results in an increased activation volume. This picture is completed by the related activation energies, since plastic deformation mediated by dislocation–grain boundary interaction usually exhibits activation energies well below 1.0 eV [34, 48]. This is consistent with the results obtained for ufg W5Re and W10Re above 600 K. For ufg W, however, where significant grain growth occurred, the measured activation energy of 2.0 to 3.0 eV is closer to the value for grain boundary diffusion (around 3.9 eV [63]) that is responsible for grain growth.

Conclusion

Ultra-fine-grained W and two binary W–Re alloys were investigated using advanced high temperature nanoindentation techniques to examine thermally activated deformation mechanisms over a broad range of temperatures. W, W5Re, and W10Re were deformed by high-pressure torsion to receive similar grain sizes (250 to 280 nm) and grain boundary characteristics. Upon annealing grain growth for ufg W starts at around 873 K, while alloying with Re suppresses it up to 1173 K. This can be attributed to a pinning effect of the grain boundaries due to solute atoms. Consequently, a steady decrease of hardness over temperature for W was observed, while the microstructural stability of the W–Re alloys allows for a distinct athermal hardness plateau above 0.15–0.2 T_m.

Comparison with results obtained on cg W and W–Re alloys shows good agreement of the transition temperature between thermal and athermal evolution of hardness, activation volume, and activation energy below 0.2 T_m. While this suggests that the kink-pair mechanism also controls plasticity of the ufg samples, the absence of a clear effect of Re on the Peierls potential in the ufg W–Re alloys, suggests a shift of the rate controlling mechanisms at the submicron scale. While still being subject to further research, it appears that local chemical effects for dislocations interacting with grain boundaries below 0.2 T_m can be more dominant than previously recognized.

Above 0.2 T_m dislocation–grain boundary mechanisms clearly become the rate controlling process, as evident from measured activation volumes and energies. The predominant processes are the interaction and accommodation of lattice dislocations with/at the grain boundaries. As their kinetics are determined by the boundary diffusivity, these processes will proceed facilitated above a certain temperature, explaining the enhanced strain rate dependence. Generally, Re shifts this increase in strain rate sensitivity to higher temperatures, consistent with intergranular stress relaxation scaling inversely with the grain boundary diffusion coefficient.

Methodology

Three different alloy compositions W, W5Re, and W10Re were provided by Plansee SE (Reutte, Austria) in a recrystallized state. The as-received samples were cut by electrical discharge machining into discs of 8 mm diameter and 1.2 mm in height. To receive an ufg microstructure these discs were subsequently deformed via high-pressure torsion [10, 64] at 673 K applying a nominal pressure of 7.5 GPa at a rotation speed of 0.2 rpm. Elevated processing temperatures are required, as deformation of W by HPT is a difficult task owing to its high strength, going along with low ductility. Uniform deformation and grain refinement during HPT is, however, only possible as long as the strength of the sample remains below that of the anvils [65]. Alloying generally reduces the achievable grain size upon HPT, thus increases the strength, allowing only limited strains in the case of W–Re alloys before slippage occurs. Therefore, depending on the alloy, different equivalent plastic strains were achieved according to Eq. 2 [45, 66], where n is the number of rotations, t the sample thickness, and r the radius from the center of the disc. All microstructural as well as nanoindentation investigations on the HPT deformed samples were carried out in the axial direction of the discs after the samples were mechanically ground and mechano-chemically polished.

$$\varepsilon = \frac{2\pi n}{\sqrt{3}t} \cdot r \qquad (2)$$

Micrographs of the material subjected to HT nanoindentation, including BSE images and EBSD-based grain orientation maps, were acquired on a high-resolution field emission SEM FEI Versa 3D DualBeam (Thermo Fisher Scientific, Waltham, MA), equipped with an EDAX Hikari XP EBSD system (EDAX Inc., Mahwah, NJ). BSE images were recorded at 10 kV, while EBSD maps were acquired at 30 kV with a step size of 10 nm.

Static heat treatments were performed in a high vacuum furnace (HTM Reetz GmbH, Berlin, Germany) at a base pressure of $< 5.0 \times 10^{-6}$ mbar. Samples were heated at a heating rate of 10 K min^{-1} until the desired temperature was reached, followed by a holding segment of 120 min before cooling back to RT at a rate of 10 K min^{-1}. A similar holding time was used as stabilization time during the high temperature nanoindentation experiments. Ufg W samples were annealed at 723, 773, 873, and 1073 K, ufg W5Re at 773, 923, 1073, 1173, and 1273 K and ufg W10Re at 973, 1073, 1173, and 1273 K. After the heat treatments, RT nanoindentation experiments were performed on a G200 platform (KLA, Milpitas, CA). The system is equipped with a continuous stiffness measurement (CSM) unit, enabling the measurement of contact stiffness, thus hardness and Young's modulus, continuously over indentation depth. All tests were performed at a constant indentation strain rate [67] of $\dot{P}/P = 0.05$ s^{-1}. A diamond Berkovich tip (Synton-MDP, Nidau, Switzerland) was used for these experiments.

Hardness values are averaged between 500 and 1400 nm indentation depth. The microstructural evolution of the annealed samples was investigated using a QUANTAX EBSD-SEM system (Bruker Nano GmbH, Berlin, Germany) equipped to a LEO 1525 at 20 kV (Carl Zeiss Microscopy GmbH, Jena, Germany) using a step size of 40 nm. Around 2000 grains were measured for grain size evaluation. The equivalent strain, see Eq. 2, of the annealed materials was 17.5 for ufg W, 17.5 for ufg W5Re, and 2.5 for ufg W10Re, respectively.

HT nanoindentation experiments were performed on an InSEM-HT (Nanomechanics Inc. KLA, Oak Ridge, TN) with a CSM unit and a separately heated tip and sample to ensure an isothermal contact. The superimposed sinusoidal force signal had a frequency of 100 Hz and a displacement amplitude of 2 nm. The system is installed in a Tescan Vega3 SEM (Tescan, Brno, Czech Republic) under high vacuum conditions ($< 5.0 \times 10^{-4}$ mbar). This excludes oxidation of the sample or degradation of the indenter at elevated temperatures [68] while at the same time allowing precise indent positioning as well as maintaining of the indentation process. A silicon carbide Berkovich tip (Synton-MDP, Nidau, Switzerland) was used for all high temperature experiments. Calibration of the frame stiffness and area function of the tip was performed by indentation tests on a reference sample of fused quartz at RT according to the analysis of Oliver and Pharr [69]. An additional tip temperature calibration was carried out by direct indentation into a thermocouple, as introduced by Wheeler and Michler [70]. After every tested sample additional indentations on fused quartz were performed to account for any possible degradation of the tip.

The nanoindentation experiments were performed from RT up to 1073 K in steps of 100 K. Young's modulus and hardness of the materials were obtained from experiments with constant indentation strain rate [67] $\dot{P}/P = 0.4\,\text{s}^{-1}$, with the reported values being averaged between 300 and 450 nm depth. The maximum indentation depth was either limited by the maximum force of 50 mN or a maximum indentation depth of 500 nm. In that case, the remaining indent is an equilateral triangle with an edge length of around 3.8 μm, thus covering a significant amount of grain boundaries in the ufg materials.

$$m = \frac{\partial(\ln(H))}{\partial(\ln(\dot{\varepsilon}))} \tag{3}$$

$$V^* = \frac{C^* \cdot \sqrt{3} \cdot k_B \cdot T}{m \cdot H}. \tag{4}$$

Additional strain rate jump tests, as introduced by Maier et al. [71], were performed to deduce strain rate sensitivity m and apparent activation volume V^*. For that purpose the indentation strain rate was kept constant at $\dot{P}/P = 0.4\,\text{s}^{-1}$ until a displacement of 300 nm, followed by an abrupt change to $\dot{P}/P = 0.04\,\text{s}^{-1}$

for 80 nm and finally switching back to $\dot{P}/P = 0.4\,\text{s}^{-1}$ for another 80 nm. From the resulting change in hardness m and V^* can be calculated according to Eqs. 3 and 4 with the Boltzmann constant k_B. The materials were investigated at different equivalent strains, namely, 26.8 for ufg W, 16.5 for ufg W5Re, and 2.4 for ufg W10Re. However, despite these differences, the three samples could be synthesized with similar grain sizes and grain boundary characters.

Open access

References

1. E. Hall, The deformation and ageing of mild steel: III. Discussion of results. Proc. Phys. Soc. B **64**(9), 747 (1951)
2. N. Petch, The cleavage strength of polycrystals. J. Iron. Steel. I**(174)**, 25–28 (1953)

3. R.Z. Valiev, T.G. Langdon, Principles of equal-channel angular pressing as a processing tool for grain refinement. Prog. Mater. Sci. **51**(7), 881–981 (2006)

4. A. Zhilyaev, T. Langdon, Three-dimensional representations of hardness distributions after processing by high-pressure torsion. Prog. Mater. Sci. **53**, 893–979 (2008)

5. Y. Saito, H. Utsunomiya, N. Tsuji, T. Sakai, Novel ultra-high straining process for bulk materials—development of the accumulative roll-bonding (ARB) process. Acta Mater. **47**(2), 579–583 (1999)

6. R.Z. Valiev, R.K. Islamgaliev, I.V. Alexandrov, Bulk nanostructured materials from severe plastic deformation. Prog. Mater. Sci. **45**(2), 103–189 (2000)

7. H. Gleiter, Nanostructured materials: basic concepts and microstructure. Acta Mater. **48**(1), 1–29 (2000)

8. J. Weertman, D. Farkas, K. Hemker, H. Kung, M. Mayo, R. Mitra, H. Van Swygenhoven, Structure and mechanical behavior of bulk nanocrystalline materials. MRS Bull. **24**(2), 44–53 (1999)

9. K. Kumar, H. Van Swygenhoven, S. Suresh, Mechanical behavior of nanocrystalline metals and alloys. Acta Mater. **51**(19), 5743–5774 (2003)

10. R. Pippan, S. Scheriau, A. Taylor, M. Hafok, A. Hohenwarter, A. Bachmaier, Saturation of fragmentation during severe plastic deformation. Ann. Rev. Mater. Res. **40**, 319–343 (2010)

11. H. Bolt, V. Barabash, W. Krauss, J. Linke, R. Neu, S. Suzuki, N. Yoshida, Materials for the plasma-facing components of fusion reactors. J. Nucl. Mater. **329**, 66–73 (2004)

12. T. Tanno, M. Fukuda, S. Nogami, A. Hasegawa, Microstructure development in neutron irradiated tungsten alloys. Mater. Trans. **52**(7), 1447–1451 (2011)

13. P. Norajitra, L. Boccaccini, A. Gervash, R. Giniyatulin, N. Holstein, G. Ihli, G. Janeschitz, W. Krauss, R. Kruessmann, V. Kuznetsov, Development of a helium-cooled divertor: material choice and technological studies. J. Nucl. Mater. **367**, 1416–1421 (2007)

14. R.A. Causey, T.J. Venhaus, The use of tungsten in fusion reactors: a review of the hydrogen retention and migration properties. Phys. Scripta **2001**(T94), 9 (2001)

15. S. Wurster, R. Pippan, Nanostructured metals under irradiation. Scripta Mater. **60**(12), 1083–1087 (2009)

16. H. Kurishita, Y. Amano, S. Kobayashi, K. Nakai, H. Arakawa, Y. Hiraoka, T. Takida, K. Takebe, H. Matsui, Development of ultrafine grained W-TiC and their mechanical properties for fusion applications. J. Nucl. Mater. **367**, 1453–1457 (2007)

17. G. Geach, J. Hughes, Plansee proceedings. Plansee Proc. XXI **I**, 245–253 (1956)

18. W. D. Klopp, Review of ductilizing of group VIA elements by rhenium and other solutes, NASA TN D-4955

19. M. Gilbert, J.-C. Sublet, Neutron-induced transmutation effects in W and W-alloys in a fusion environment. Nucl. Fusion **51**(4), 043005 (2011)

20. L. Romaner, C. Ambrosch-Draxl, R. Pippan, Effect of rhenium on the dislocation core structure in tungsten. Phys. Rev. Lett. **104**(19), 195503 (2010)

21. J. Kappacher, A. Leitner, D. Kiener, H. Clemens, V. Maier-Kiener, Thermally activated deformation mechanisms and solid solution softening in W–Re alloys investigated via high temperature nanoindentation. Mater. Des. **189**, 108499 (2020)

22. A. Argon, *Strengthening Mechanisms in Crystal Plasticity*, vol. 4 (Oxford University Press, Oxford, 2008)

23. Y. Li, X. Zeng, W. Blum, Transition from strengthening to softening by grain boundaries in ultrafine-grained Cu. Acta Mater. **52**(17), 5009–5018 (2004)

24. J. May, H. Höppel, M. Göken, Strain rate sensitivity of ultrafine-grained aluminium processed by severe plastic deformation. Scripta Mater. **53**(2), 189–194 (2005)

25. H. Höppel, J. May, P. Eisenlohr, M. Göken, Strain-rate sensitivity of ultrafine-grained materials. Z. Metallkd. **96**(6), 566–571 (2005)

26. M.A. Meyers, A. Mishra, D.J. Benson, Mechanical properties of nanocrystalline materials. Prog. Mater. Sci. **51**(4), 427–556 (2006)

27. H. Conrad, Plastic deformation kinetics in nanocrystalline fcc metals based on the pile-up of dislocations. Nanotechnology **18**(32), 325701 (2007)

28. Q. Wei, S. Cheng, K. Ramesh, E. Ma, Effect of nanocrystalline and ultrafine grain sizes on the strain rate sensitivity and activation volume: fcc versus bcc metals. Mat. Sci. Eng. A **381**(1–2), 71–79 (2004)

29. J. Su, Z.-B. Tang, C.-X. Wang, T. Ye, T. Suo, Y.-L. Li, Compressive behavior and deformation kinetics of ultrafine grained aluminum processed by equal channel angular pressing. Int. J. Smart Nano Mater. **8**(1), 56–77 (2017)

30. L. Hollang, E. Hieckmann, D. Brunner, C. Holste, W. Skrotzki, Scaling effects in the plasticity of nickel. Mater. Sci. Eng. A **424**(1–2), 138–153 (2006)

31. T. Suo, Y.-L. Li, K. Xie, F. Zhao, K.-S. Zhang, Q. Deng, Experimental investigation on strain rate sensitivity of ultra-fine grained copper at elevated temperatures. Mech. Mater. **43**(3), 111–118 (2011)

32. N. Isaev, T. Grigorova, P. Zabrodin, Strain-rate sensitivity of the flow stress of ultrafine-grain aluminum at temperatures 4.2–295 K. Low Temp. Phys. **35**(11), 898–904 (2009)

33. N. Ahmed, A. Hartmaier, Mechanisms of grain boundary softening and strain-rate sensitivity in deformation of ultrafine-grained metals at high temperatures. Acta Mater. **59**(11), 4323–4334 (2011)

34. O. Renk, V. Maier-Kiener, I. Issa, J. Li, D. Kiener, R. Pippan, Anneal hardening and elevated temperature strain rate sensitivity of nanostructured metals: their relation to intergranular dislocation accommodation. Acta Mater. **165**, 409–419 (2019)

2417

35. A. Seeger, The temperature and strain-rate dependence of the flow stress of body-centred cubic metals: A theory based on kink–kink interactions. Z. Metallkd. **72**(6), 369–380 (1981)

36. B. Sestak, A. Seeger, Gleitung und Verfestigung in kubisch-raumzentrierten Metallen und Legierungen. Z. Metallkd. **69**(4), 195–202 (1978)

37. V. Maier, A. Hohenwarter, R. Pippan, D. Kiener, Thermally activated deformation processes in body-centered cubic Cr - How microstructure influences strain-rate sensitivity. Scripta Mater. **106**, 42–45 (2015)

38. D. Wu, X. Wang, T. Nieh, Variation of strain rate sensitivity with grain size in Cr and other body-centred cubic metals. J. Phys. D Appl. Phys. **47**(17), 175303 (2014)

39. R. Fritz, D. Wimler, A. Leitner, V. Maier-Kiener, D. Kiener, Dominating deformation mechanisms in ultrafine-grained chromium across length scales and temperatures. Acta Mater. **140**, 176–187 (2017)

40. Q. Wei, T. Jiao, K. Ramesh, E. Ma, Nano-structured vanadium: processing and mechanical properties under quasi-static and dynamic compression. Scripta Mater. **50**(3), 359–364 (2004)

41. D. Kiener, R. Fritz, M. Alfreider, A. Leitner, R. Pippan, V. Maier-Kiener, Rate limiting deformation mechanisms of bcc metals in confined volumes. Acta Mater. **166**, 687–701 (2019)

42. J. May, H. W. Höppel, M. Göken, Strain rate sensitivity of ultrafine grained fcc-and bcc-type metals, in: Mater. Sci. Forum, Vol. 503, Trans Tech Publ, pp. 781–786 (2006)

43. Q. Wei, T. Jiao, K. Ramesh, E. Ma, L. Kecskes, L. Magness, R. Dowding, V. Kazykhanov, R. Valiev, Mechanical behavior and dynamic failure of high-strength ultrafine grained tungsten under uniaxial compression. Acta Mater. **54**(1), 77–87 (2006)

44. V. Maier, C. Schunk, M. Göken, K. Durst, Microstructure-dependent deformation behaviour of bcc-metals-indentation size effect and strain rate sensitivity. Phil. Mag. **95**(16–18), 1766–1779 (2015)

45. T. Hebesberger, H. Stüwe, A. Vorhauer, F. Wetscher, R. Pippan, Structure of cu deformed by high pressure torsion. Acta Mater. **53**(2), 393–402 (2005)

46. R. Lowrie, A. Gonas, Dynamic elastic properties of polycrystalline tungsten, 24–1800 °C. J. Appl. Phys. **36**(7), 2189–2192 (1965)

47. E. Savitskii, M. Tylkina, S. Ipatova, E. Pavlova, Properties of tungsten-rhenium alloys. Met. Sci. Heat. Treat. **2**(9), 483–486 (1960)

48. D.-H. Lee, I.-C. Choi, G. Yang, Z. Lu, M. Kawasaki, U. Ramamurty, R. Schwaiger, J.-I. Jang, Activation energy for plastic flow in nanocrystalline cocrfemnni high-entropy alloy: a high temperature nanoindentation study. Scripta Mater. **156**, 129–133 (2018)

49. F.J. Humphreys, M. Hatherly, *Recrystallization and Related Annealing Phenomena* (Elsevier, Oxford, 2012)

50. B.D. Beake, A.J. Harris, J. Moghal, D.E. Armstrong, Temperature dependence of strain rate sensitivity, indentation size effects and pile-up in polycrystalline tungsten from 25 to 950 °C. Mater. Des. **156**, 278–286 (2018)

51. R. Ayres, G. Shannette, D. Stein, Elastic constants of tungsten-rhenium alloys from 77 to 298 K. J. Appl. Phys. **46**(4), 1526–1530 (1975)

52. S. Bonk, J. Hoffmann, A. Hoffmann, J. Reiser, Cold rolled tungsten (W) plates and foils: evolution of the tensile properties and their indication towards deformation mechanisms. Int. J. Refract. Met. Hard Met. **70**, 124–133 (2018)

53. A. Leitner, V. Maier-Kiener, D. Kiener, Extraction of flow behavior and hall-petch parameters using a nanoindentation multiple sharp tip approach. Adv. Eng. Mater. **19**(4), 1600669 (2017)

54. S. Nemat-Nasser, W. Guo, M. Liu, Experimentally-based micromechanical modeling of dynamic response of molybdenum. Scripta Mater. **40**(7), 859–872 (1999)

55. S. Nemat-Nasser, W. Guo, Flow stress of commercially pure niobium over a broad range of temperatures and strain rates. Mater. Sci. Eng. A **284**(1–2), 202–210 (2000)

56. D. Brunner, Comparison of flow-stress measurements on high-purity tungsten single crystals with the kink-pair theory. Mater. Trans. **41**(1), 152–160 (2000)

57. A. Giannattasio, S.G. Roberts, Strain-rate dependence of the brittle-to-ductile transition temperature in tungsten. Philos. Mag. **87**(17), 2589–2598 (2007)

58. L. Dezerald, L. Proville, L. Ventelon, F. Willaime, D. Rodney, First-principles prediction of kink-pair activation enthalpy on screw dislocations in bcc transition metals: V, Nb, Ta, Mo, W, and Fe. Phys. Rev. B **91**(9), 094105 (2015)

59. H. Li, C. Draxl, S. Wurster, R. Pippan, L. Romaner, Impact of d-band filling on the dislocation properties of bcc transition metals: the case of tantalum-tungsten alloys investigated by density-functional theory. Phys. Rev. B **95**(9), 094114 (2017)

60. P.L. Raffo, Yielding and fracture in tungsten and tungsten-rhenium alloys. J. Less Common M. **17**(2), 133–149 (1969)

61. Y. Cui, G. Po, N. Ghoniem, Temperature insensitivity of the flow stress in body-centered cubic micropillar crystals. Acta Mater. **108**, 128–137 (2016)

62. L. Priester, On the accommodation of extrinsic dislocations in grain boundaries. Interface Sci. **4**(3–4), 205–219 (1997)

63. H. Mehrer, *Diffusion in Solid Metals and Alloys*, vol. 26 (Landolt-Börnstein, New Series, 1990)

64. O. Renk, R. Pippan, Saturation of grain refinement during severe plastic deformation of single phase materials: reconsiderations, current status and open questions. Mater. Trans. **60**(7), 1270–1282 (2019)

65. M. Wurmshuber, S. Doppermann, S. Wurster, D. Kiener, Ultrafine-grained tungsten by high-pressure torsion-bulk precursor versus powder processing route. IOP Conf. Ser. Mat. Sci. **580**, 012051 (2019)

66. H.P. Stüwe, Equivalent strains in severe plastic deformation. Adv. Eng. Mater. **5**(5), 291–295 (2003)

67. B. Lucas, W. Oliver, Indentation power-law creep of high-purity indium. Metall. Mater. Trans. A **30**(3), 601–610 (1999)

68. J. Wheeler, D. Armstrong, W. Heinz, R. Schwaiger, High temperature nanoindentation: the state of the art and future challenges. Curr. Opin. Solid State Mater. **19**(6), 354–366 (2015)

69. W.C. Oliver, G.M. Pharr, An improved technique for determining hardness and elastic modulus using load and displacement sensing indentation experiments. J. Mater. Res. **7**(6), 1564–1583 (1992)

70. J. Wheeler, J. Michler, Elevated temperature, nano-mechanical testing in situ in the scanning electron microscope. Rev. Sci. Instrum. **84**(4), 045103 (2013)

71. V. Maier, K. Durst, J. Mueller, B. Backes, H.W. Höppel, M. Göken, Nanoindentation strain-rate jump tests for determining the local strain-rate sensitivity in nanocrystalline Ni and ultrafine-grained Al. J. Mater. Res. **26**(11), 1421–1430 (2011)